Journal of Colloid and Interface Science 339 (2009) 285–295

Contents lists available at ScienceDirect

Journal of Colloid and Interface Science

www.elsevier.com/locate/jcis

The effects of nanoparticle aggregation processes on aggregate structure and metal uptake

Benjamin Gilbert [a,*], Reyn K. Ono [b], Kristen A. Ching [b], Christopher S. Kim [b,*]

[a] Earth Science Division, Lawrence Berkeley National Laboratory, Berkeley, CA, USA
[b] Department of Chemistry, Chapman University, Orange, CA, USA

ARTICLE INFO

Article history:
Received 20 March 2009
Accepted 20 July 2009
Available online 28 July 2009

Keywords:
Adsorption
Aggregation
Desorption
EXAFS
Nanoparticle
SAXS

ABSTRACT

Adsorption at the mineral–water interface is an important process governing metal ion concentration and mobility in aqueous systems. Ferric iron oxyhydroxide nanoparticles possess a large capacity for the adsorption of heavy metals but quantification of metal uptake and sequestration is challenging due to the tendency of natural nanoparticles to aggregate in natural waters. We studied the effects of aggregation via pH, ionic strength, drying, and freezing on the uptake and release of copper from ferrihydrite nanoparticles employing small-angle X-ray scattering (SAXS) studies of aggregate morphology, macroscopic Cu(II) sorption and desorption batch experiments, and extended X-ray absorption fine structure (EXAFS) spectroscopic studies of copper sorption geometries. Results show that the mechanism of aggregation has a large effect upon aggregate morphology and consequently on the net sorption/retention of ions from solution. While aggregation reduces the total amount of copper that can be adsorbed, it also may introduce physical constraints to desorption and/or increased proportions of higher strength binding sites that lead to greater retention, and hence more effective sequestration, of metal ion contaminants.

1. Introduction

Nanoscale oxide and oxyhydroxide minerals are widespread in the natural environment, and their formation or introduction can significantly affect the chemistry of surface waters, groundwater, sediments and soils [1–4]. Ferric iron-bearing nanomaterials, particularly ferrihydrite, can efficiently adsorb and sequester aqueous ions including nutrients such as phosphates and contaminants such as heavy metals [5–8] and radionuclides [9,10], and this capacity may be valuable for the remediation of waters contaminated by species such as copper or zinc [11,12]. After formation in natural aqueous systems however, nanomaterials typically undergo aggregation, which mediates their environmental impact by altering their transport properties and the ways that their surfaces can participate in surface sorption processes.

Previous investigators have identified several specific mechanisms by which aggregation may control the rate and extent of the uptake and sequestration of aqueous ions. In particular, while metal sorption onto ferrihydrite is characterized by rapid initial uptake, a longer timescale increase in quantitative uptake has been observed and interpreted as being due to pore [13] or surface [14,15] diffusion, or by slow precipitation reactions [16]. However, the fate of sorbates in aggregates involves coupled processes occurring within porous media for which structural models are presently lacking. Nanoparticle aggregates are two-phase (water–solid) materials with complex three-dimensional (3D) structures that cannot be visualized directly by conventional electron or X-ray imaging methods [14,17]. Although gas adsorption methods can quantify surface area and pore dimensions in porous materials, these methods require complete drying of the materials and often involve outgassing in vacuum, which can alter pore morphology. By contrast, recent studies have shown that the structures of aggregates can be investigated *in situ* by small-angle X-ray scattering (SAXS). Model-independent analysis methods can provide quantitative determination of pore size distributions [18,19], porosity and surface area [20]. In addition, while it is not possible to directly invert SAXS data to uniquely determine 3D aggregate structure, visualization methods have been developed that can generate representations of particle aggregates and pore morphologies consistent with the data.

We combined SAXS-based structural analysis methods with solution studies of metal uptake to study the structure and metal uptake behavior of ferrihydrite nanoparticles aggregated by a range of pathways summarized in Table 1. This involved subjecting monodisperse nanoparticle suspensions to analogs of natural aggregation processes, including: pH variation around the point of zero surface charge (simulating the neutralization of acid mine drainage); changes in ionic strength (simulating mixing of fresh and saline water); and drying and freezing at several temperatures.

* Corresponding authors. Address: Department of Chemistry, Schmid College of Science, Chapman University, One University Drive, Orange, CA 92866, USA. Fax: +1 714 532 6048.
E-mail address: cskim@chapman.edu (C.S. Kim).

0021-9797/$ - see front matter © 2009 Elsevier Inc. All rights reserved.
doi:10.1016/j.jcis.2009.07.058

Table 1
Summary of methods used to aggregate ferrihydrite nanoparticles, and the surface areas of control and aggregated samples measured by BET after air drying at room temperature (20 °C).

Control		pH variation		Ionic strength variation		Drying		Freezing	
Control	S.A. (m^2/g)	pH	S.A. (m^2/g)	[$NaNO_3$] (M)	S.A. (m^2/g)	Drying temperature (°C)	S.A. (m^2/g)	Freezing temperature (°C)	S.A. (m^2/g)
pH 5, 1 mM $NaNO_3$	305	6	330	0.01	303	30	328	−4	324
		7	–	0.1	308	50	352	−70	325
		8	379	1.0	275	75	280	−193	293
		9	–						
		10	436						

Aggregate morphology was investigated using *in situ* small-angle X-ray scattering for quantitative characterization of pore size, porosity and surface area. Visualization methods were employed to generate statistically representative examples of the aggregate morphologies that provide additional insight into the physical constraints on aqueous ion transport within aggregates. We also studied the speciation of copper sorbed to the various aggregates using extended X-ray absorption fine structure (EXAFS) spectroscopy, concluding that spectroscopic analysis of the sorption species is crucial for developing accurate models of how metal ions are sequestered by nanoparticle aggregates.

2. Experimental methods

2.1. Sample preparation and characterization

Aqueous suspensions of iron oxyhydroxide nanoparticles with mean diameter approximately 5 nm and solids concentration of 6.74 g L^{-1} were synthesized using a microwave flash synthesis (forced hydrolysis) method [21]. The suspensions were cleaned by dialysis in 1000 Dalton molecular weight cut-off (MWCO) membranes for several days against deionized water until reaching pH 5.0. Portions of the suspensions were subsequently dialyzed for three days against a solution of 0.001 M $NaNO_3$, periodically replacing the solution to guarantee a constant pH 5.0. One aliquot was left in this control solution while the others were aggregated using the methods described in the following section.

The initially synthesized nanoparticles were air-dried and then further outgassed at 90 °C under a constant flow of dry He gas for a period of 12 h before measuring the surface area by the BET method using a Beckman Coulter SA3100 surface area analyzer; the non-aggregated particles were determined to be 305 m^2/g. The point of zero net surface charge of these nanoparticles in solutions in equilibrium with atmospheric CO_2 was previously measured by potentiometric titration to be approximately pH_{znsc} = 8.6 [22].

2.2. Nanoparticle aggregation

The solution chemistry of one sample series was adjusted with 0.001 M NaOH to pH values between 6.0 and 10.0 at room temperature. The ionic strength of a separate sample series was increased by dialyzing the particles against solutions at pH 5 and 0.001 (control), 0.01, 0.1, and 1.0 M $NaNO_3$ at room temperature. Both of these sample series were allowed to aggregate for a period of 1 week. Another sample series was dried in open air at 30 °C, 50 °C and 75 °C using conventional laboratory ovens. A final sample series was frozen in a commercial freezer at −4 °C, in an ultra-cold freezer at −70 °C, and by immersion in liquid nitrogen at −193 °C. The frozen samples were allowed to thaw and the dried samples were initially re-immersed in the appropriate volume of DI water to restore the initial solids concentration following drying. All aggregated samples were returned to the initial control aqueous conditions (pH 5.0 and 0.001 M $NaNO_3$) by dialysis for 2 days, replacing the control solution multiple times each day, prior to the subsequent copper uptake experiments. Visual observation indicated that the aggregated nanoparticles were not re-dispersed following re-equilibration with the control solution, in agreement with prior feasibility studies. The surface areas of dried aliquots of all aggregates were measured using BET surface area analysis. Table 1 summarizes aggregation conditions undertaken in this study and the associated BET measurements.

2.3. Small-angle X-ray scattering (SAXS) experiments

The morphologies of hydrated aggregates were studied using *in situ* small-angle X-ray scattering (SAXS) at 8.33 keV at beamline 1–4 of the Stanford Synchrotron Radiation Lightsource (SSRL). The samples were confined between 2 mica windows separated by 0.5 mm, and the transmission was measured using ionization detectors situated before and after the sample holder. The transmission was measured prior to and after each measurement to check for settling. In order to maximize the range of scattering angle and q, SAXS data were acquired with the sample placed in two positions relative to the stationary two-dimensional detector (Roper). The sample-detector distances were calibrated using chicken collagen and silver behemate samples for the low-q and high-q positions, respectively. The 2D SAXS patterns recorded by the detector were binned onto a 1D q-axis using the Nika code in IgorPro software and corrected for incident flux and sample transmission. For each sample, the background intensity caused by scattering from air, helium, the mica windows and water were subtracted. The low-q scattering was normalized to absolute intensity units using a lupollen reference [23] with a known scattering cross-section (6 cm^{-1} at 0.025 $Å^{-1}$) and the high-q data were scaled by an arbitrary constant to overlap the two SAXS patterns.

2.4. SAXS data analysis

2.4.1. Analysis of fractal aggregate geometry

Many aggregation processes lead to the formation of fractal structures that can be described by geometric parameters related to the physical mechanism of aggregation. Most importantly, the aggregate fractal dimension defines the scaling relationship between mass (or particle number) and enclosed volume, and is a measure of how efficiently the particles are packed [24]. Numerous investigators have used small-angle scattering (SAS) methods to study the geometry of aggregates of colloidal particles in solutions because it provides a direct measure of the fractal dimension [24–26]. Following Teixeira [27], we describe the SAXS structure factor, $S(q)$, for fractal aggregates of spherical particles of radius a and fractal dimension, d_f, by:

$$S(q) = 1 + \frac{1}{(qa)^{d_f}} \frac{2a\Gamma(a-1)}{(a-1)} \sin\left[(a-1)\tan^{-1}(q\xi)\right] \left(1 + \frac{1}{(q\xi)^2}\right), \quad (1)$$

where $\Gamma(a-1)$ is the gamma function and ξ is the large-size cut-off in the aggregate density distribution function. A log-normal size distribution of particle sizes (obtained from a fit to SAXS data from low-pH, dispersed dilute nanoparticles) is incorporated numerically.

2.4.2. Visualization of fractal clusters

Insights into aggregation processes have been obtained by simulating the growth of aggregates by the addition of new particles or clusters to a growing aggregate. In studies that attempt to simulate aggregate growth processes, the structures of the resulting aggregates are determined by computational parameters, such as sticking efficiencies that represent particular physical or chemical factors [28]. In the present work, however, we adopted an alternative strategy in which aggregates are constructed in such a way that the fundamental fractal scaling relation is constrained at every growth step [29,30]. The fractal scaling law for aggregates containing N identical primary particles is expressed:

$$N = k_f \left(\frac{R_g}{a}\right)^{D_f}, \tag{2}$$

where k_f is the fractal prefactor, a is the primary particle radius, D_f is the fractal dimension, and the radius of gyration, R_g, is related to the mean square of the distances between the particle positions, $\mathbf{r}_i$, and the geometrical center of mass of the aggregate at $\mathbf{r}_o$:

$$R_g^2 = \frac{1}{N}\sum_{i=1}^{N}(\mathbf{r}_i - \mathbf{r}_o). \tag{3}$$

This strategy ensures that when a particle or a cluster is added to an existing cluster the distance between their centers of mass, Γ, must satisfy:

$$\Gamma^2 = \frac{a(N_1+N_2)^2}{N_1N_2}\left(\frac{N_1+N_2}{k_f}\right)^{2/D_f} - \frac{(N_1+N_2)}{N_2}R_1^2 - \frac{(N_1+N_2)}{N_1}R_2^2, \tag{4}$$

where N_n and R_n are the particle number and radius of gyration of the nth cluster. In this way, the fractal scaling law is satisfied at every step. We modified the off-lattice method described by Filipov to incorporate a range of particle sizes chosen randomly from a log-normal distribution by re-expressing Eqs. (2)–(4) in terms of the *mass* of a particle or cluster rather than the *number* of primary particles. Thus, we could generate models of small nanoparticle aggregates using parameters (nanoparticle size and size distribution; aggregate size; and fractal dimension) obtained from fits to the SAXS data. This method permitted the relationship between aggregate structure and the associated small-angle scattering patterns to be investigated in a systematic fashion. The SAXS pattern for each model aggregate was calculated using the Debye equation [31]. At least 50 clusters were generated for a given set of parameters, and the calculated SAS patterns were averaged for comparison with the experimental data.

2.4.3. Analysis of porous granular medium geometry

Granular porous material contains porosity on at least two spatial scales [20,32]. The aggregates formed by drying and freezing consist of micron-scale grains with intergrain voids of similar dimensions but possessing interior porosity on the nanometer scale. In the present work we focused on characterizing the nanoscale porosity, which is associated with the vast majority of the sample surface area. The size and size distribution of the nanoscale pores was estimated by fitting the simulated SAXS pattern for spheres with a log-normal distribution of radii. We estimated the internal porosity of these aggregates using an approach described by Spalla et al. [20]. Because we fully rewetted the aggregates before the SAXS studies, we assume both the micro- and nanoscale pores to be filled with water. The solid:water volume fraction, η, may be calculated from the measured transmission, T, of the X-ray beam through the sample holder of known thickness:

$$\eta = (\mu_{tot} - \mu_{water})/(\mu_{solid} - \mu_{water}), \tag{5}$$

where $\mu_{tot} = -\ln(T)/\delta$. At 8.33 keV, $\mu_{water} = 8.9\ \mathrm{cm}^{-1}$ and $\mu_{ferrihydrite} = 714\ \mathrm{cm}^{-1}$, assuming the stoichiometry of ferrihydrite to be $Fe_{10}O_{16}H_2$ [33].

While the precise lineshape of SAXS data obtained from an arbitrary material depends on structure within the material, it is well established that an integral quantity called the *invariant, Q,* is related only to the X-ray scattering strength of the material and independent of morphology [34]. For a homogeneous porous material,

$$Q = \int_0^\infty I(q)q^2, \tag{6}$$

and the pore-solid porosity, ϕ, is given by $\phi = Q/2\pi^2\Delta\rho^2$, where $\Delta\rho$ is the X-ray scattering contrast between the solid and pore phases. There are two additional steps for a granular porous material. First, the experimental scattering intensity must be divided by the volume fraction. Second, the scattering associated with the fine pores must be extracted from the experimental data by fitting a Porod function to the low-q region and subtracting this from the entire pattern. For the present calculations, $\Delta\rho = \rho_{ferrihydrite} - \rho_{water}$, where at 8.33 keV $\rho_{ferrihydrite} = 35.4\ \mathrm{cm}^{-2}$ and $\rho_{water} = 9.5\ \mathrm{cm}^{-2}$. All the steps of this analysis are reported graphically below.

Analysis of the high-q Porod region additionally provides an estimate of the total surface area,

$$\sum = \lim_{q\to\infty} I(q)q^4/2\pi\Delta\rho^2, \tag{7}$$

where for granular porous media the experimental intensity is again divided by the volume fraction. We employed a method described by Hedström et al. to generate models of two-phase porous materials with interior geometries consistent with the SAXS data [35].

2.5. Copper(II) adsorption and desorption

Preliminary copper uptake experiments were performed on a non-aggregated sample at a solids concentration of $2.25\ \mathrm{g\ L^{-1}}$ to determine appropriate parameters (pH values for total copper uptake and significant desorption, initial Cu(II) concentration) for subsequent experiments. Following aggregation and re-equilibration of the prepared nanoparticle suspensions with the control solution at pH 5.0 and 0.001 M $NaNO_3$, batch Cu(II) adsorption and subsequent desorption experiments were performed. Adsorption experiments were performed on 40 mL solutions containing 6.7 mg of nanoparticles ($0.17\ \mathrm{g\ L^{-1}}$, corresponding to a surface area of approximately $2.0\ \mathrm{m^2}$) at pH 6.0 and with 0.5 mM $Cu(NO_3)_2$ for a 24 h equilibration period. The copper-sorbed nanoparticles were separated from the solution by centrifuging at 3000 RPM for 15 min followed by filtration of the decanted supernatants through 0.2 μm filters. The resulting supernatants were acidified with small volumes of concentrated HNO_3 to pH < 2 and analyzed for residual $Cu(II)_{(aq.)}$ concentrations using a Thermo Scientific Solar atomic absorption (AA) spectrometer and Cu(II) calibration standards prepared under the same experimental conditions. Supernatants were also analyzed for $Fe(III)_{(aq.)}$ concentrations using AA spectroscopy and found to be negligible, verifying that nanoparticles were effectively removed from solution through the centrifugation and filtration steps. Solids were retained for later EXAFS analysis.

The desorption studies were performed on separate but parallel sample series to the adsorption studies. Following 24 h Cu(II) adsorption, the solutions were adjusted to pH 5.0 using 0.1 M HNO_3 and rotated for a period of 30 min. Preliminary studies in

which desorption was conducted for 30 min and 90 min showed no difference in the extent of desorption, so it is assumed that the easily-desorbed fraction was removed after 30 min. The suspensions were centrifuged, filtered, acidified, and analyzed by AA spectroscopy in the same manner as with the supernatants generated from the adsorption experiments, and solids were retained for later EXAFS analysis.

Triplicate adsorption and desorption experiments were conducted on the control (non-aggregated) nanoparticles in order to assess the degree of error between individual repeat experiments following both the adsorption and desorption steps. These calculated errors, which were calculated to be 0.83% for the adsorption experiments and 2.21% for the desorption experiments, are expected to be representative of the range of error in the macroscopic experiments.

2.6. Extended X-ray absorption fine structure (EXAFS) spectroscopy

Samples were loaded as moist pastes into Teflon sample holders and sealed with Kapton tape. Cu *K*-edge EXAFS spectra were collected at SSRL on beamline 11-2 using Si(220) monochromator crystals at room temperature in the fluorescence-yield mode and a 30-element, high-throughput germanium detector. This method is optimized for low-concentration samples [36] and enabled the collection of high-quality EXAFS spectra from ferrihydrite samples following both the adsorption and desorption steps. Aluminum filters served to attenuate background matrix fluorescence from the iron in the sample. Energy calibration was conducted for each scan through the use of a Cu foil placed downstream of the sample and by assigning the first inflection point of the absorption *K*-edge of the foil to an energy value of 8979.0 eV.

EXAFS scans were averaged and processed using the Sixpack data analysis software package [37]. Phase and amplitude functions of single-shell scattering paths for Cu–O and Cu–Fe scattering interactions were generated using FEFF 6 [38] and subsequently utilized in quantitative fitting of the background-subtracted spectra and corresponding Fourier transforms. The scale factor was fixed at 0.9 for all samples and the Debye–Waller factor, which serves as a measure of thermal vibration and static disorder around the Cu in the sample, was set at values appropriate to those of sorption complexes (e.g. 0.01 $Å^2$ for second-shell neighbors) based on our previous studies on comparable sorption systems [39,40]. Multiple scattering effects were not considered in this study.

3. Results

3.1. Surface area analysis of dried aggregates

Portions of most aggregated samples and the control suspension were dried in air for BET surface area analysis, as reported in Table 1. With the obvious exceptions of the samples aggregated by drying, we anticipate that preparing the samples for gas adsorption analysis alters the surface area relative to that accessible in aqueous solution (SA^{aq}). Nevertheless, we observe some trends in the measured BET surface areas (SA^{BET}). We observe an increase in SA^{BET} with drying temperature from approximately 20 °C (the control sample that was not aggregated before analysis) to 50 °C. The subsequent loss of surface area found for the material dried at 75 °C suggests that particle growth occurred at this temperature [2]. Unexpectedly, a substantial increase in SA^{BET} was found for the samples in which pH was increased, even though light and X-ray scattering as well as direct visual observation showed that this caused extensive aggregation. As discussed below, this is compatible with the hypothesis that certain pathways create aggregates in solution with higher accessible surface areas than obtained when drying, and that drying pre-formed aggregates at least partly preserves these more open aggregate structures. Certain pathways, such as aggregation in 1 M $NaNO_3$, create aggregates with less surface area than obtained by drying. Overall, the results show that SA^{BET} may not always correlate with SA^{aq} and emphasize the view that novel methods of surface area determination in solution will be required to correctly interpret the rates of interfacial phenomena involving nanoscale particles [41,42]. The SAXS studies below represent the first steps in applying this method for *in situ* surface area and pore morphology analysis of analogues of natural samples.

3.2. SAXS analysis of aggregation by pH and ionic strength variation

Fig. 1 summarizes the SAXS data acquired from the control suspension of non-aggregated nanoparticles and from samples aggregated by changing solution chemistry (pH, ionic strength). The SAXS profile for the control sample is consistent with a suspension of non-aggregated individual particles with a distribution of particle sizes. The weak peak at $q \approx 0.01$ $Å^{-1}$ indicates that at pH 5 the nanoparticles experience mutual repulsive interactions. The repulsive electrostatic interactions originate from the positive surface charge that forms when $pH < pH_{znsc}$, preventing

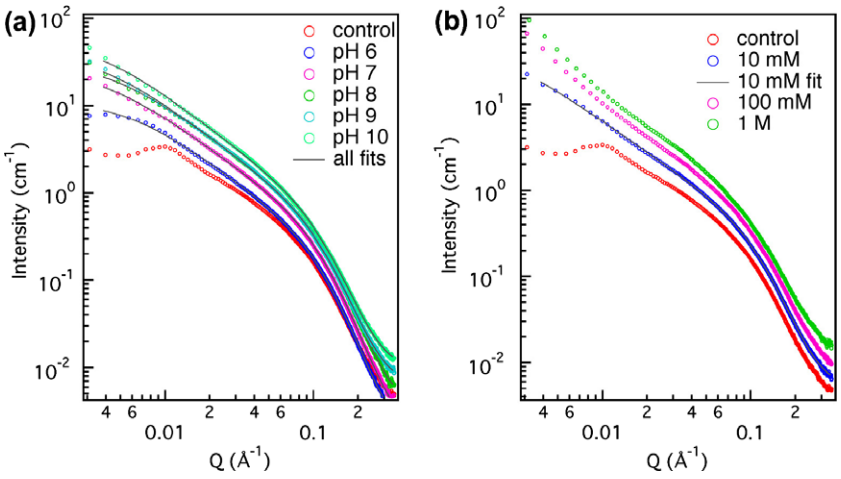

Fig. 1. Small-angle X-ray scattering data from iron oxyhydroxide nanoparticles in suspension at pH 5 and 10^{-3} M $NaNO_3$ (control, red circles) and aggregated by a variety of methods. (a) Aggregation by pH increase. (b) Aggregation by ionic strength increase. (For interpretation of color mentioned in this figure legend, the reader is referred to the web version of the article.)

aggregation. Increasing either the pH or the ionic strength causes aggregation by, respectively, lowering the magnitude of the surface charge, or by shielding it. Aggregation is clearly identified in the SAXS data by the strong increase in scattering intensity at low-q. The intensity increase is accompanied by the development of a linear region in the log–log plots of Fig. 1, showing that the aggregates possess fractal geometry. Fractal aggregates are also formed when the ionic strength is increased. The range of object sizes that can be determined by a SAXS experiment is limited by the q-range of the scattering data, with the largest size determined by the minimum q via $d_{max} \approx 2\pi/q_{min}$. In the present data, while q_{min} is too high for accurate aggregate size analysis for all samples, the aggregate size appears to become larger when ionic strength is increased, because, in contrast to the pH data, these curves show no sign of reaching an intensity plateau. Table 2 summarizes the geometric parameters fitted to these data.

We used an algorithm to generate fractal aggregates consisting of primary particles with the same size and size distribution of the ferrihydrite nanoparticles studied in this work, with the goal of creating 3D models that are consistent with the SAXS data. The q-range accessed by the present SAXS data is sufficient to completely describe only the smallest clusters generated in this study, and hence we report in Fig. 2 an example cluster generated for the pH 6 data. The cluster shown is 1 of 50 for which the average of the simulated SAXS patterns is in close agreement to the data. The structural model emphasizes the conclusion obtained from the fitting results: that the nanoparticle aggregates adopt very open structures that are unlikely to substantially reduce the surface area accessible to aqueous ions. Fits to the experimental SAXS data indicate that, while the aggregate size increases with solution pH, the fractal dimension stays approximately constant. Hence, the larger structures that form under higher pH conditions are likely to be loose aggregates of nanoparticle clusters [43] that are similar to the one illustrated in Fig. 2. We previously observed that these aggregates are very stable over more than 3 months [22] in the absence of hydrodynamic shear stress (e.g. stirring) that may cause restructuring and compaction [44,45].

3.3. SAXS analysis of aggregation by drying and freezing

Fig. 3 reports SAXS data for samples aggregated by drying and freezing. The SAXS lineshapes for all of these samples are distinct from those found for the pH and ionic strength series, indicating a substantively different type of aggregate geometry relative to the solution phase aggregates. These SAXS data are typical for materials that are granular and porous, and indicate that these aggregation pathways create a compact two-phase material with nanoscale internal porosity; we analyzed the data of Fig. 3 using this assumption. The SAXS data treatment steps required to extract the pore scattering component and determine the pore scattering invariant are presented in Fig. 4 and the analysis results are summarized in Table 3.

Table 2
Results of fitting a fractal aggregate model to SAXS data acquired from nanoparticles aggregated by varying solution pH and ionic strength. The aggregates are described by two parameters: the fractal dimension, $1 < D_f < 3$, a measure of the efficiency with which the nanoparticles are packed, and the cut-off parameter, ϵ, a measure of the largest cluster sizes attained. The data q-range does not support fitting ϵ for the 0.1 M and 1 M ionic strength samples.

	pH variation					Ionic strength variation		
	pH 6	pH 7	pH 8	pH 9	pH 10	10^{-2} M	10^{-1} M	1 M
D_f	1.40	1.38	1.41	1.43	1.44	1.32	1.33	1.37
ϵ (nm)	20	29	26	29	31	67	–	–

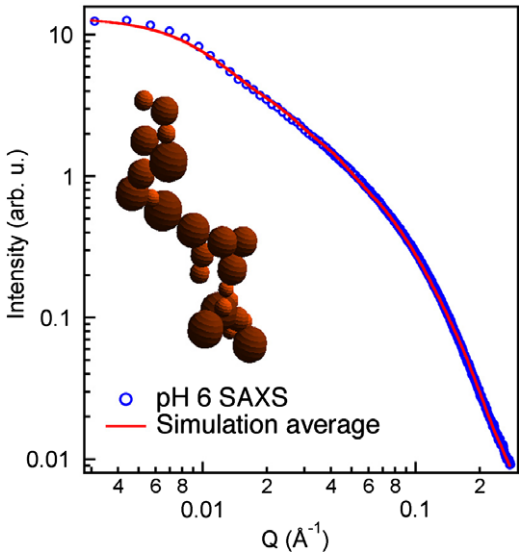

Fig. 2. Simulated model of the nanoparticle clusters formed by aggregation in solution at pH 6. Structural models were formed using an algorithm that constructs fractal clusters with primary particle size and size distribution, and fractal dimension obtained from fitting the experimental SAXS data. The size of the cluster was varied manually by changing the number of particles in the simulated clusters to achieve agreement in the low-q regime.

The SAXS data reveal a complex dependence of aggregate structure on drying temperature. The aggregates formed at 30 °C are more compact than those formed at higher temperatures and the pore dimensions increase with drying temperature. At 75 °C the grain size is larger and there is a loss of total surface area likely due to aggregation-based growth [46]. Inspection of the pore scattering curves in Fig. 4 reveal the presence of a distinct correlation peak (at approximately 0.06 Å^{-1}) only in the 50 °C data. This indicates that locations of the pores in the aggregates are not uncorrelated, with the development of a preferred average pore–pore distance. For the dried samples, the trend in SA^{SAXS} with increasing temperature is in reasonable agreement with the trend in SA^{BET} although additional work is required to be able to establish confident limits on surface area analysis with SAXS. Freezing temperature exerts a relatively small effect upon aggregate structure, although we find that the greatest range of pore sizes is created at the lowest temperature (−193 °C).

While the SAXS data analysis approach described above provides geometric parameters such as pore dimensions and surface areas, the properties of a porous medium depend strongly on the arrangement of pores in 3D space. We employed a numerical approach to generate 3D structures with disordered pore morphologies consistent with the extracted pore scattering component of the SAXS data [35]. This approach was originally developed for the purpose of visualizing pore morphologies in nanoporous polymer films, but is equally valid for any isotropic, nanoscale, two-phase material. Two-dimensional cross sections through 3D models generated in this way are presented in Fig. 5. As with any method that generates 3D structures from 1D scattering data, the resulting structure is not unique and may not be optimal [47,48]. Moreover, the fine-scale resolution is limited by the $50 \times 50 \times 50$ cubic grid used in the simulation. Nevertheless, these models provide important insights into pore connectivity that cannot be obtained from simple fitting methods. We analyzed the connectivity of the pores in the structures shown in Fig. 5 and found all to be fully interconnected. Only in the 30 °C structure were a few isolated pores identified. These represented a tiny fraction of total porosity (<0.1%), and were preferentially located close to the simulation boundaries.

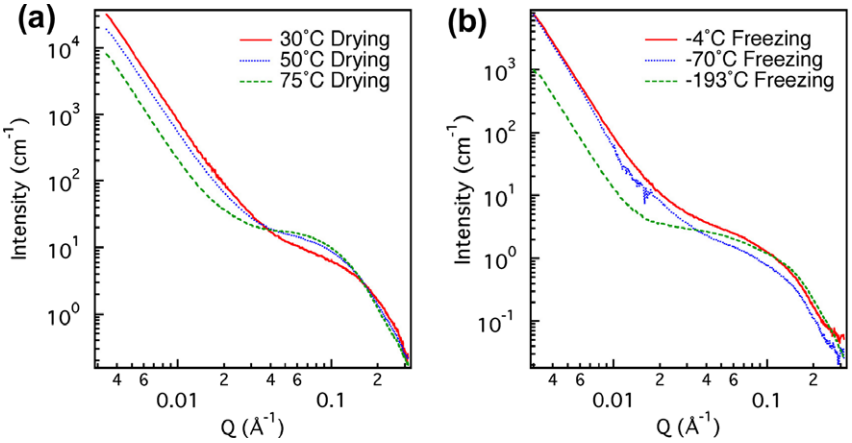

Fig. 3. Small-angle X-ray scattering data from iron oxyhydroxide nanoparticles aggregated by drying and freezing at the temperatures indicated. (a) SAXS data from dried and rehydrated samples. (b) SAXS data from frozen samples following thawing and rehydration. The structure in the −70 °C data in the 0.01–0.02 Å^{-1} region is spurious noise associated with high X-ray absorption and low scattering intensity from a sample that was thicker than optimal.

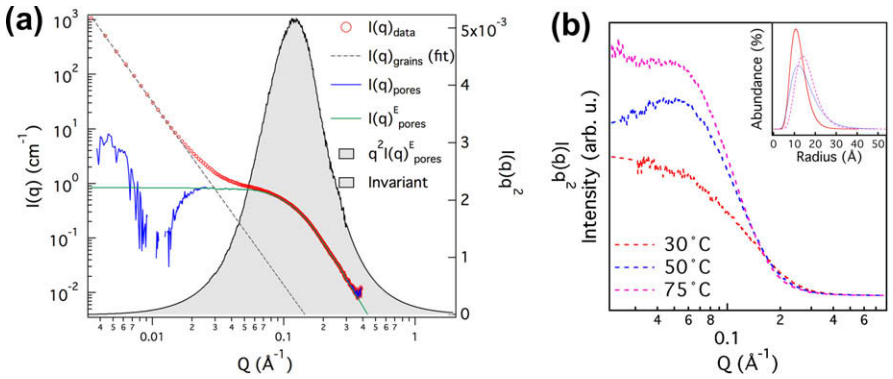

Fig. 4. (a) Graphical representation of the SAXS data analysis for calculating the invariant associated with scattering from the internal porosity of the nanoparticle aggregates. The experimental data, $I(q)_{data}$, must first be treated so that it is given in absolute scattering units, as described in the text. The low-q region exhibits a characteristic q^4 dependency associated with Porod scattering from the surface of larger granular aggregates. Subtraction of this component leaves the scattering associated only with the intra-aggregate pores, $I(q)_{pores}$. This curve is extrapolated to $q = 0$ and $q \to \infty$ to give the extracted pore scattering curve $I(q)^{E}_{pores}$. The function $q^2 I(q)^{E}_{pores}$ is plotted *vs.* the right axis and the invariant is the shaded area under this curve. (b) Comparison of the pore scattering curves, $I(q)^{E}_{pores}$, obtained for samples dried at the indicated temperatures. Inset: fitted pore size distributions.

Table 3
Results of analysis of the SAXS data from nanoparticle aggregates formed by drying and freezing at the temperatures indicated. The nanoscale porosity was calculated from the scattering invariant. BET surface area data is duplicated from Table 1.

	Drying			Freezing		
	30 °C	50 °C	75 °C	−4 °C	−70 °C	−193 °C
Mean pore radius (nm)	1.2	1.4	1.5	1.6	1.6	1.3
Pore distribution width[a]	0.3	0.4	0.3	0.35	0.34	0.38
Porosity (%)	32	50	74	64	–[b]	78
Surface area (SAXS) (m^2g^{-1})	303	374	261	–[c]	–[c]	–[c]
Surface area (BET) (m^2g^{-1})	328	352	280	324	325	293

[a] Assuming log-normal distribution of pore sizes.
[b] Due to sample settling, quantitative porosity determination was not possible.
[c] Due to low signal in the high-q SAXS data from the frozen samples, quantitative surface area determination was not possible.

3.4. Quantitative copper adsorption and desorption experiments

We performed copper adsorption and desorption experiments to investigate the effects of particle aggregation on heavy metal ion sequestration. The experimental conditions were chosen after acquiring copper uptake data on non-aggregated particles as a function of pH and Cu(II) concentration. The data in Fig. 6a and b are similar to prior studies of copper sorption onto ferric iron oxyhydroxides [49–51]. The copper adsorption isotherm (Fig. 6b) shows that sorption was performed far from saturation coverage without loss of soluble Cu via (co)precipitation.

Fig. 7 reports the percentage uptake of the added Cu(II) by the dispersed, non-aggregated nanoparticle (control) sample and by the samples in which aggregation was induced by different mechanisms prior to Cu(II) exposure. These measurements show that aggregation typically results in reduced Cu(II) uptake relative to the non-aggregated control sample; that the amount of uptake varies for different aggregation processes; and that the degree of uptake approximately

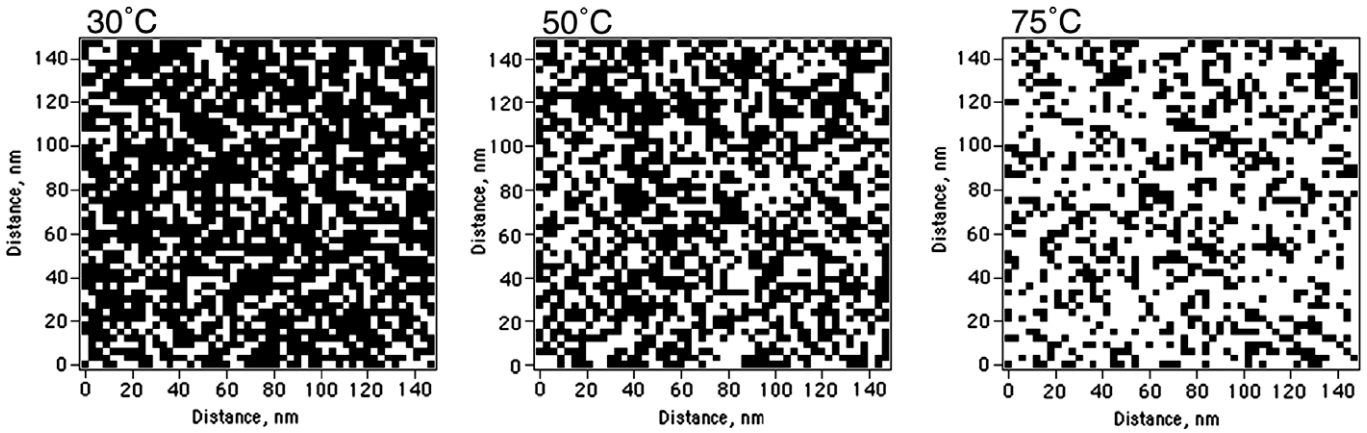

Fig. 5. Visualizing representative structures of aggregates formed by drying nanoparticle suspensions at the indicated temperatures. Each panel presents a cross-section through a 3D model of pore morphology reconstructed from SAXS data using the approach of Hedström et al. [35]. Black = solid (nanoparticle) phase.

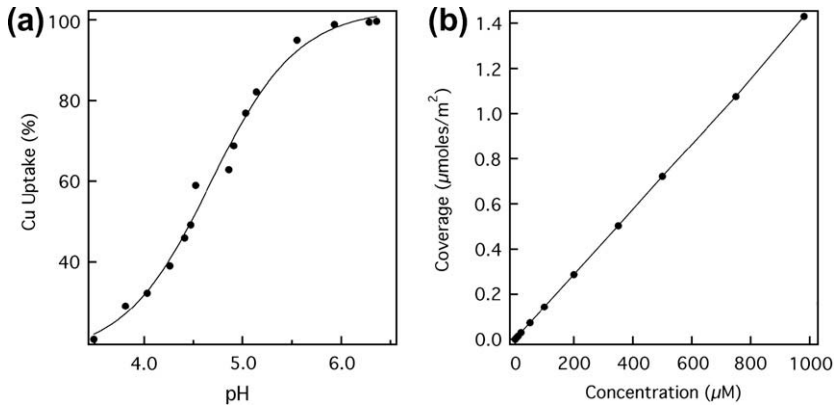

Fig. 6. (a) Copper uptake curve showing the pH dependence of Cu(II) sorption onto iron oxyhydroxide nanoparticles. The smooth line is a guide to the eye. (b) Copper adsorption isotherm showing the uptake as a function of aqueous Cu(II) concentration at pH 6 and 0.17 g L^{-1} solids concentration.

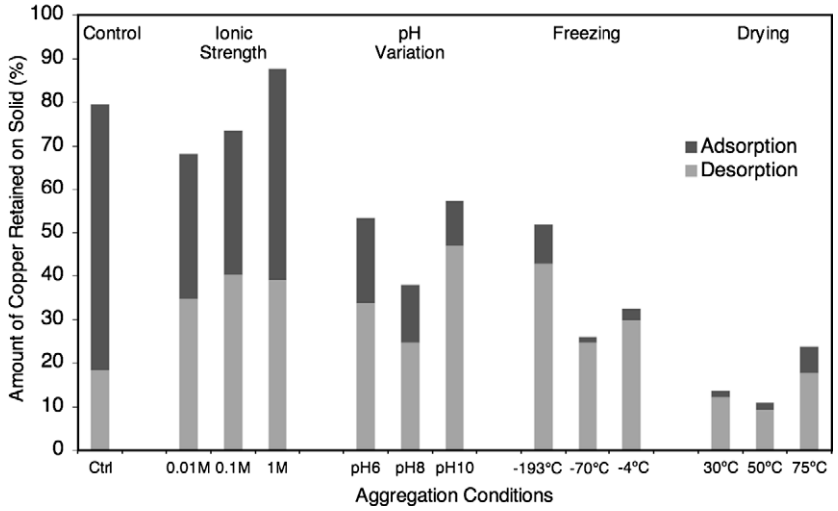

Fig. 7. The uptake and release of aqueous divalent copper ions by iron oxyhydroxide nanoparticles both dispersed (control) and aggregated by a variety of methods. Copper adsorption and retention are expressed as a percentage of the initial Cu(II) introduced in solution at pH 6.0. Estimated errors for adsorption and desorption values are 0.8% and 2.2% respectively, based on triplicate experiments for dispersed control nanoparticles.

decreases in the order: ionic strength > pH > freezing > drying. Fig. 7 also reports the amount of copper retained on (and thus gives the amount desorbed from) the control and the aggregates when the pH was lowered to a value of 5.0, expressed again as a percentage of the initially introduced Cu(II). The differences in copper sorption observed for samples aggregated by different pathways are

substantially greater than the experimental uncertainties measured by separate triplicate uptake and release trials using the control nanoparticle suspension. These data therefore indicate that samples exhibiting lower capacities for adsorption due to aggregation also retain a larger proportion of the adsorbed copper ions.

3.5. EXAFS analysis of copper adsorption geometries

Fits of the Cu *K*-edge EXAFS spectra and corresponding Fourier transforms for sorption samples generated from the control and two of the nanoparticle aggregate suspensions (1.0 M ionic strength, pH 10) are shown in Fig. 8, with fitting results provided in Table 4. For each sample, spectra were collected and fit following both the initial adsorption step and the subsequent desorption step, and qualitative differences between the different spectra can be observed in Fig. 8. Specifically, more pronounced shoulders are visible at $k \sim 7.8$ and 11.0 $Å^{-1}$ in the EXAFS spectra following desorption compared to the respective spectra following adsorption. Consequently, an increase in the amplitude of the second-neighbor Fourier transform features is apparent in the 2.3–3.3 Å region (uncorrected for phase shift) for samples following desorption relative to those following adsorption.

The quantitative fitting results in Table 4 agree with the qualitative differences observed in the EXAFS spectra and Fourier transforms. In all cases the nearest neighbor to the average Cu atom in the sample is oxygen with a coordination number between 3.3–3.7 (±0.4) Å at an average distance of 1.95 (±0.01) Å. Although copper is typically hexa–aquo coordinated in solution, Jahn–Teller distortion of the $Cu(H_2O)_6$ octahedron removes the degeneracy of the Cu(II) $3d^9$ electron ground state and the first shell is dominated by the four equatorial oxygens [52]. This is in agreement with prior room temperature studies of Cu(II) sorption to mineral surfaces [14,53]. Two second-neighbor features were also identified in all spectra and fitted with Cu–Fe scattering interactions at average distances of 3.02 (±0.01) and 3.29 (±0.02) Å. The shorter distance is consistent with Cu ions forming inner-sphere sorption complexes either as dimers in binuclear corner-sharing configurations or in mononuclear bidentate edge-sharing configurations with the $Fe(O,OH)_6$ octahedra that comprise the substrate [53]. The longer distance is consistent primarily with mononuclear bidentate inner-sphere sorption complexes in corner-sharing configurations with the $Fe(OH)_6$ octahedra, as observed in other EXAFS studies of Cu(II) on iron hydroxide substrates [14,53]. Fig. 9 illustrates these and other copper binding geometries that may be present following adsorption. The coordination environments generated from fitting of the EXAFS spectra are not consistent with the structural environment of copper in $Cu(OH)_{2(s)}$. This observation, combined with our Cu(II) sorption isotherm (Fig. 6b), which does not indicate a sharp increase in sorbed Cu(II) at our designated uptake experimental conditions, suggests that the (surface) precipitation of $Cu(OH)_{2(s)}$ is not a significant process in our samples.

No significant changes in the first oxygen shell coordination number at 1.95 Å are observed in any of the data. In contrast, the average coordination numbers of both the second-shell (3.02, 3.29 Å) Fe neighbors increase following the desorption step. Notably, the quantitative changes in these second-shell coordination numbers are not proportional for the three samples; specifically, in the sample order listed the percentage change in the 3.29 Å coordination number increases while the change in the 3.02 Å feature drops. This reinforces our interpretation of these contributions as representing distinct surface species with alternative sorption geometries. The EXAFS data from all three samples can therefore be interpreted as representing different proportions of a minimum of three distinct surface species: outer sphere $Cu(OH)_6$ and two inner-sphere species, likely mononuclear edge-sharing and corner-sharing bidentate species. Thus, an important conclusion of the spectroscopic analysis is that aggregate morphology can have a detectable effect on the balance of surface speciation.

4. Discussion

The data show that the mechanism of aggregation has a major impact on the aggregate morphology (interior structure and porosity), and that these properties strongly affect the ability of

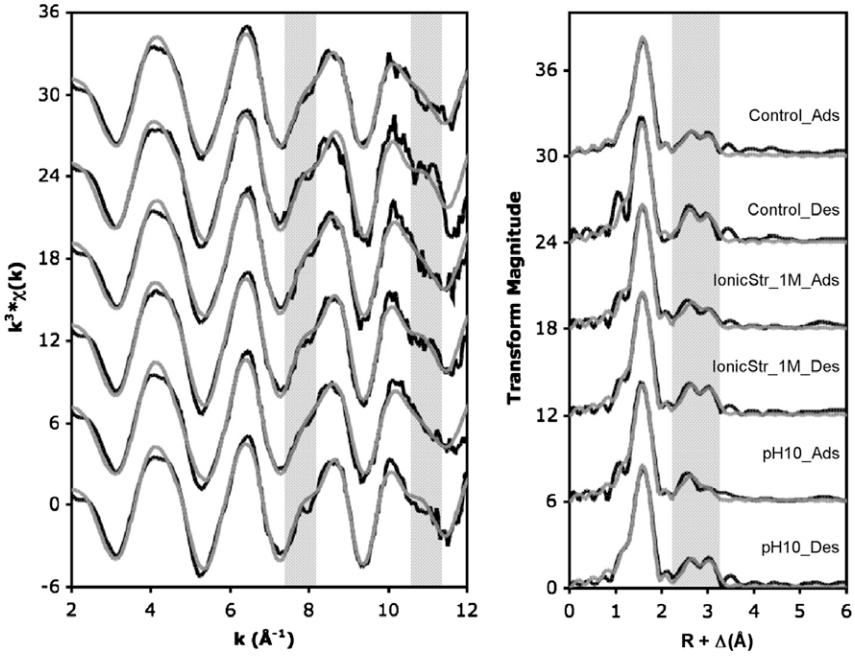

Fig. 8. Fits of the k^3-weighted Cu *K*-edge EXAFS data and corresponding Fourier transforms (black lines = raw data, gray lines = fit) for Cu(II) sorbed on control (non-aggregated) ferrihydrite nanoparticles and nanoparticles aggregated through increased ionic strength or pH. For each sample, spectra were collected following both the initial adsorption step and the subsequent desorption step. Shaded regions show the areas of the EXAFS spectra and Fourier transforms where differences can be identified between the adsorption and desorption spectra.

Table 4
Cu *K*-edge EXAFS fitting results for Cu(II) sorption samples (see Fig. 8 for corresponding EXAFS spectra and Fourier transforms), including coordination numbers (CN), interatomic distances (R), and Debye–Waller factors (σ^2). Also included is the change in coordination number between the sample fitting results after the adsorption step and after the desorption step.

Sample	Cu–O				Cu–Fe				Cu–Fe			
	CN	% Change in CN	R(Å)	σ^2(Å^2)	CN	% Change in CN	R(Å)	σ^2(Å^2)	CN	% Change in CN	R(Å)	σ^2(Å^2)
Control Ads	3.4(2)		1.96(1)	0.004(1)	1.6(3)		3.02(1)	0.01[a]	1.5(4)		3.30(2)	0.01[a]
Control Des	3.6(4)	4	1.95(1)	0.004(1)	2.4(6)	51	3.01(1)	0.01[a]	2.4(8)	61	3.27(2)	0.01[a]
I.S.[b] 1 M Ads	3.3(3)		1.95(1)	0.003(1)	1.7(4)		3.01(1)	0.01[a]	1.3(5)		3.29(2)	0.01[a]
I.S.[b] 1 M Des	3.7(3)	11	1.95(1)	0.004(1)	2.2(4)	30	3.03(1)	0.01[a]	2.3(5)	71	3.29(1)	0.01[a]
pH10 Ads	3.6(3)		1.95(1)	0.004(1)	1.6(4)		3.00(1)	0.01[a]	1.0(5)		3.27(3)	0.01[a]
pH10 Des	3.6(3)	2	1.96(1)	0.004(1)	2.1(4)	31	3.03(1)	0.01[a]	2.2(5)	122	3.30(1)	0.01[a]

Notes: Standard deviations at a 95% confidence level are listed in parentheses.
[a] Value fixed in least-squares refinement.
[b] I.S. = ionic strength.

nanoscale particles to adsorb and sequester aqueous ions. An important distinction may be made between aggregation processes that occur in liquid water (pH and ionic strength increases) and those that involve the removal of water from aggregate structures (drying and freezing), with the latter processes leading to the formation of compact nanoporous aggregates that have a lower capacity for aqueous ion adsorption than the more open fractal structures generated during the former processes.

Among the solution phase results, nanoparticles that are aggregated by increasing pH create fractal aggregates with a higher fractal dimension than those that are aggregated by increasing the ionic strength. The higher fractal dimension indicates closer packing, and this is associated with a lower capacity for metal uptake. At present, it is uncertain how to estimate the loss of surface area that accompanies fractal aggregate formation, but we are exploring methods of surface area estimation from aggregate models such as that in Fig. 2.

In agreement with prior observations [14,54], drying the suspensions is particularly effective for reducing the capacity for metal uptake. The estimates of surface area obtained from gas adsorption and the SAXS data are not in close quantitative agreement, but they do exhibit similar variation with drying temperature. Moreover, the trends in surface area do not clearly match the trends in metal sorption since within the temperature series, for example, the greatest uptake is observed for the 75 °C sample, which has the lowest surface area (likely due to some particle growth). However, as drying temperature increases both the mean pore size and the overall porosity increases, leading to a closer relationship between these parameters and observed metal uptake.

The results of the EXAFS studies contribute additional insight into the mechanism of metal sequestration within ferrihydrite aggregates. These studies reveal that the retained copper atoms are surrounded by a greater number of iron neighbors after desorption has taken place. If a single mode of copper sorption dominated throughout the adsorption and desorption processes, one would expect the coordination numbers for each shell to remain relatively unchanged save for an overall decline in data quality in the desorption samples due to an overall reduced copper concentration. Thus, we infer that the desorption step removes a higher proportion of one or more weakly-bound species than the more strongly-bound species that remain following desorption.

The presence of Cu–Fe coordination numbers in excess of 2.0 (the maximum expected from a bidentate corner-sharing surface sorption complex) suggests that more entrained forms of copper persist following desorption. These entrained species would feature higher average Cu–Fe coordination numbers, such as copper ions that have been structurally incorporated into the nanoparticle's near-surface lattice or trapped/sorbed within interparticle pore spaces of larger aggregates as shown schematically in Fig. 9. More work is required to determine whether the alternate binding configurations represent distinct surface sites on one [33] or more [55,56] phases in ferrihydrite, migration into nanopores at the interface between aggregated nanoparticles, or incorporation into growing nanocrystals.

Our results show that aggregation state is an important factor for the long-term sequestration of copper and likely other contaminant species with an affinity for ferric iron oxyhydroxide nanoparticles. The loss of surface area is an important factor limiting the

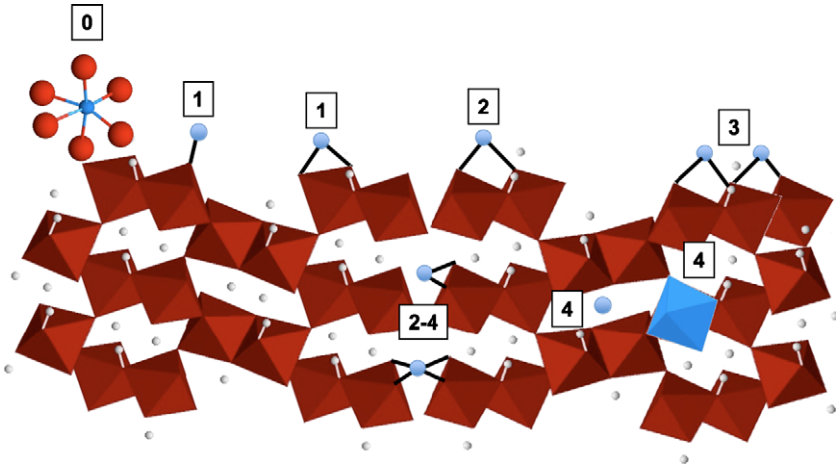

Fig. 9. Schematic representation of potential metal ion sorption complexes. For simplicity, in most cases the coordinating oxygen ions are not shown around the metal cations. Boxed values indicate the possible number of Fe or Cu second-neighbors within the distance range observed in the experimental EXAFS.

capacity of nanoparticle aggregates for adsorbing aqueous ions, but the drop in surface area alone cannot account for the trends on copper uptake and retention. Our 3D reconstructions of aggregate morphology indicate that the formation of isolated pores that would limit accessible surface area does not significantly occur. Thus, we conclude that the lower capacity for uptake is due both to surface area loss and a substantial reduction in the net transport of aqueous ions into the most compact aggregates. Simulation studies using the pore morphologies generated in the present work are presently underway to quantify the extent to which pore structure attenuates diffusion rates.

A striking observation of the present study is that, following desorption of the more weakly-bound sorbates, the distribution of surface binding geometries varies with aggregate morphology. The batch sorption/desorption studies combined with the EXAFS investigations reveal that, while aggregation may reduce the total amount of sorbate that can be adsorbed, physical constraints on desorption (e.g. trapped or pore-bound metal species) and/or increased proportions of higher strength binding sites can lead to the increased retention, and hence more effective sequestration, of metal ion contaminants.

5. Conclusions

The aggregation of iron oxyhydroxide nanoparticles by pathways occurring in the natural environment causes the formation of nanoporous materials that vary significantly in both pore and aggregate morphology. When aqueous ions diffuse into aggregates and adsorb to sites on the internal aggregate surfaces, the net uptake is diminished for materials with lower porosity and smaller pore dimensions, indicating that physical loss of accessible surface area is the dominant factor that alters uptake capacity. Specifically, the transition from low-aggregation states (control) to intermediate (ionic strength-induced) and higher (pH-induced) aggregation states correlates with both declining degrees of total Cu(II) uptake, lower amounts of Cu(II) desorption (i.e. greater retention), and increasing proportions of Cu(II) ions in more stable binding modes, including the possibility of more strongly structurally-incorporated configurations.

The present study shows, however, that simple geometric parameters (surface area; porosity; pore dimensions) are not sufficient to quantitatively explain the effects of aggregation on uptake and release, indicating that full insight into this process requires understanding how aggregate morphology affects the mobility of aqueous ions within the pore network. Studies of diffusion within aggregates requires 3D models that accurately represent pore geometry and connectivity, and we have shown that SAXS methods may provide an approach to deriving accurate geometric models. Because the pore dimensions are nanoscale, models of diffusion will likely require the incorporation of interfacial phenomena such as the development of surface charge and counterion layers [57], and the ordering of water molecules [58]. In addition to the physical constraints on aqueous ion transport in nanoporous aggregates, a complete picture of metal sequestration by such materials also requires a molecular-level understanding of the chemical interactions between sorbates and the nanoparticle surfaces, as well as their reaction kinetics.

Acknowledgments

This work was supported by the Director, Office of Science, Office of Basic Energy Sciences, Division of Chemical Sciences, Geosciences, and Biosciences, of the US Department of Energy under Contract No. DE-AC02-05CH11231, the American Chemical Society – Petroleum Research Grant, PRF #44721-GB10, Cottrell College Science Award #6940 from the Research Corporation, and the National Science Foundation, Division of Earth Sciences, Grant #061821711. Small-angle X-ray scattering experiments were performed on beamline 1–4 and the EXAFS experiments on beamline 11-2 at the Stanford Synchrotron Radiation Lightsource (SSRL) and we thank John Pople and Joe Rogers, respectively, for their assistance. We also thank Bridget Ingham and Mike Toney for advice on the generation of pore morphologies from SAXS data. Thanks also to Chapman University Environmental Geochemistry Lab members Megan McKee and Lauryn DeGreeff for their earlier studies on pH-dependent Cu(II) uptake to ferrihydrite nanoparticles which aided in the design of the macroscopic uptake experiments, Chris Lentini for help acquiring SAXS data at beamline 1–4, and James Dale for assistance in fitting of the EXAFS data and measuring the uncertainties in copper sorption experiments.

References

[1] B. Gilbert, J.F. Banfield, Mol. Geomicrobiol. 59 (2005) 109–155.
[2] G.A. Waychunas, C.S. Kim, J.F. Banfield, J. Nanoparticle Res. 7 (2005) 409–433.
[3] T.A. Kirpichtchikova, A. Manceau, L. Spadini, F. Panfili, M.A. Marcus, T. Jacquet, Geochim. Cosmochim. Acta 70 (2006) 2163–2190.
[4] C. van der Zee, D.R. Roberts, D.G. Rancourt, C.P. Slomp, Geology 31 (2003) 993–996.
[5] G.A. Waychunas, C.C. Fuller, J.A. Davis, Geochim. Cosmochim. Acta 66 (2002) 1119–1137.
[6] J.A. Dyer, P. Trivedi, N.C. Scrivner, D.L. Sparks, Environ. Sci. Technol. 37 (2003) 915–922.
[7] J.A. Dyer, P. Trivedi, N.C. Scrivner, D.L. Sparks, J. Colloid Interface Sci. 270 (2004) 56–65.
[8] L. Spadini, P.W. Schindler, L. Charlet, A. Manceau, K.V. Ragnarsdottir, J. Colloid Interface Sci. 266 (2003) 1–18.
[9] T.D. Waite, J.A. Davis, T.E. Payne, G.A. Waychunas, N. Xu, Geochim. Cosmochim. Acta 58 (1994) 5465–5478.
[10] A.P. Novikov, S.N. Kalmykov, S. Utsunomiya, R.C. Ewing, F. Horreard, A. Merkulov, S.B. Clark, V.V. Tkachev, B.F. Myasoedov, Science 314 (2006) 638–641.
[11] K.G. Karthikeyan, H.A. Elliott, J. Chorover, J. Colloid Interface Sci. 209 (1999) 72–78.
[12] J.A. Dyer, P. Trivedi, S.J. Sanders, N.C. Scrivner, D.L. Sparks, Environ. Sci. Technol. 37 (2003) 923–930.
[13] A. Hofmann, W. van Beinum, J.C.L. Meeussen, R. Kretzschmar, J. Colloid Interface Sci. 283 (2005) 29–40.
[14] A.C. Scheinost, S. Abend, K.I. Pandya, D.L. Sparks, Environ. Sci. Technol. 35 (2001) 1090–1096.
[15] L. Axe, P. Trivedi, J. Colloid Interface Sci. 247 (2002) 259–265.
[16] D.A. Dzombak, F.M.M. Morel, J. Colloid Interface Sci. 112 (1986) 588–598.
[17] R.L. Penn, C. Zhu, H. Xu, D.R. Veblen, Geology 29 (2001) 843–846.
[18] A. Hofmann, M. Pelletier, L. Michot, A. Stradner, P. Schurtenberger, R. Kretzschmar, J. Colloid Interface Sci. 271 (2004) 163–173.
[19] C.M. Goodell, B. Gilbert, S. Weigand, H. Zhang, J.F. Banfield, Geochim. Cosmochim. Acta 70 (2006) A209.
[20] O. Spalla, S. Lyonnard, F. Testard, J. Appl. Crystallogr. 36 (2003) 338–347.
[21] Y. Guyodo, A. Mostrom, R.L. Penn, S.K. Banerjee, Geophys. Res. Lett. 30 (2003) 1512.
[22] B. Gilbert, G.P. Lu, C.S. Kim, J. Colloid Interface Sci. 313 (2007) 152–159.
[23] A. Endres, U. Lode, G. vonKrosigk, M. Bark, S. Cunis, R. Gehrke, W. Wilke, Rev. Sci. Instrum. 68 (1997) 4009–4013.
[24] G.C. Bushell, Y.D. Yan, D. Woodfield, J. Raper, R. Amal, Adv. Colloid Interface Sci. 95 (2002) 1–50.
[25] R.F. Reidy, A.J. Allen, S. Krueger, J. Non-Cryst. Solids 285 (2001) 181–186.
[26] H. Wu, J.J. Xie, M. Lattuada, M. Morbidelli, Langmuir 21 (2005) 3291–3295.
[27] J. Teixeira, J. Appl. Crystallogr. 21 (1988) 781–785.
[28] M. Lattuada, H. Wu, M. Morbidelli, J. Colloid Interface Sci. 268 (2003) 106–120.
[29] R. Thouy, R. Jullien, J. Phys. A 27 (1994) 2953–2963.
[30] A.V. Filippov, M. Zurita, D.E. Rosner, J. Colloid Interface Sci. 229 (2000) 261–273.
[31] E. Pantos, H.F. vanGarderen, P.A.J. Hilbers, T.P.M. Beelen, R.A. vanSanten, J. Mol. Struct. 383 (1996) 303–308.
[32] A.J. Allen, S. Krueger, G. Skandan, G.G. Long, H. Hahn, H.M. Kerch, J.C. Parker, M.N. Ali, J. Am. Ceram. Soc. 79 (1996) 1201–1212.
[33] F.M. Michel, L. Ehm, S.M. Antao, P.L. Lee, P.J. Chupas, G. Liu, D.R. Strongin, M.A.A. Schoonen, B.L. Phillips, J.B. Parise, Science 316 (2007) 1726–1729.
[34] A. Guinier, X-Ray Diffraction, in: Crystals, Imperfect Crystals, and Amorphous Bodies, Dover Publications, 1994.
[35] J.A. Hedstrom, M.F. Toney, E. Huang, H.C. Kim, W. Volksen, T. Magbitang, R.D. Miller, Langmuir 20 (2004) 1535–1538.
[36] G.A. Waychunas, G.E. Brown Jr., Adv. X-Ray Anal. 37 (1994) 607–617.
[37] S.M. Webb Sam's Interface for XAS Package (SixPACK). <http://www-ssrl.slac.stanford.edu/swebb/index.htm>.

[38] J.J. Rehr, J.M. d. Leon, S.I. Zabinsky, R.C. Albers, J. Am. Chem. Soc. 113 (1991) 5135–5140.
[39] C.S. Kim, J.J. Rytuba, G.E. Brown Jr., J. Colloid Interface Sci. 271 (2004) 1–15.
[40] C.S. Kim, J.J. Rytuba, G.E. Brown Jr., J. Colloid Interface Sci. 270 (2004) 9–20.
[41] L.M. He, B.M. Tebo, Appl. Environ. Microbiol. 64 (1998) 1123–1129.
[42] D.M. Cwiertny, R.M. Handler, M.V. Schaefer, V.H. Grassian, M.M. Scherer, Geochim. Cosmochim. Acta 72 (2008) 1365–1380.
[43] B. Lo, T.D. Waite, J. Colloid Interface Sci. 222 (2000) 83–89.
[44] F. Le Berre, G. Chauveteau, E. Pefferkorn, J. Colloid Interface Sci. 199 (1998) 13–21.
[45] B.E. Logan, J.R. Kilps, Water Res. 29 (1995) 443–453.
[46] J.F. Banfield, S.A. Welch, H.Z. Zhang, T.T. Ebert, R.L. Penn, Science 289 (2000) 751–754.
[47] P. Chacon, J.F. Diaz, F. Moran, J.M. Andreu, J. Mol. Biol. 299 (2000) 1289–1302.
[48] D.I. Svergun, Biophys. J. 76 (1999) 2879–2886.
[49] M.M. Benjamin, J.O. Leckie, J. Colloid Interface Sci. 79 (1980) 209–221.
[50] D.A. Dzombak, F.M.M. Morel, Surface Complexation Modeling: Hydrous Ferric Oxide, John Wiley and Sons, 1990.
[51] M. Ponthieu, F. Juillot, T. Hiemstra, W.H. van Riemsdijk, M.F. Benedetti, Geochim. Cosmochim. Acta 70 (2006) 2679–2698.
[52] F.A. Cotton, G. Wilkinson, Advanced Inorganic Chemistry, Fifth ed., John Wiley and Sons, New York, NY, 1988.
[53] C.L. Peacock, D.M. Sherman, Geochim. Cosmochim. Acta 68 (2004) 2623–2637.
[54] J.Y. Bottero, M. Arnaud, F. Villieras, L.J. Michot, P. Dedonato, M. Francois, J. Colloid Interface Sci. 159 (1993) 45–52.
[55] L.J. Criscenti, D.A. Sverjensky, J. Colloid Interface Sci. 253 (2002) 329–352.
[56] V.A. Drits, B.A. Sakharov, A.L. Salyn, A. Manceau, Clay Miner. 28 (1993) 185–207.
[57] W. van Beinum, A. Hofmann, J.C.L. Meeussen, R. Kretzschmar, J. Colloid Interface Sci. 283 (2005) 18–28.
[58] S. Kerisit, D.J. Cooke, D. Spagnoli, S.C. Parker, J. Mater. Chem. 15 (2005) 1454–1462.